




Cite this: *Soft Matter*, 2022, 18, 7280

Received 6th July 2022,  
Accepted 28th August 2022

DOI: 10.1039/d2sm00913g

[rsc.li/soft-matter-journal](http://rsc.li/soft-matter-journal)

## The growth and the decay of a visco-elastocapillary ridge by localized forces†

Tak Shing Chan 

A soft solid layer develops a ridge-like deformation below the contact line due to the pulling force of the liquid–air surface tension when a droplet is in contact with it. We investigate the growth and the decay of a viscoelastic wetting ridge. The global features, e.g. the ridge height, evolve with time scales corresponding to the relaxation of the viscoelastic material. In contrast, we show that locally around the tip of the ridge, the surface tensions not only determine the equilibrium shape, but also have a significant impact on the dynamics, for which the relaxation has a characteristic spreading velocity depending on the solid surface tension. The relaxation time to an equilibrium state depends on the distance from the contact line, which can be much smaller than the long-term relaxation time scale of the viscoelastic material. The different dynamics between the global features of the ridge and the tip morphology suggests an alternative focus when investigating the contact line dynamics in soft wetting, such as stick-slip motion.

### 1 Introduction

A liquid droplet in contact with a soft substrate, such as elastomers, gels and rubbers, can deform the substrate due to the localized force acted upon by the liquid on the solid at the contact line.<sup>1,2</sup> This morphological change in soft solids has a significant impact on the shape of the droplet,<sup>3</sup> as well as the dynamical process when the droplet is in motion.<sup>4–8</sup> Apart from the scenario of droplets interacting with a soft solid, studying how soft solids respond to external localized stresses is important to the understanding of industrial and biological systems such as soft adhesion,<sup>9,10</sup> and the functions of cells and tissues.<sup>11,12</sup>

The deformation of soft solids below the contact line appears as a ridge-like shape, which has been measured, for example, using X-ray microscopy.<sup>1</sup> The equilibrium shape of the ridge is critically determined by the elastic properties of the soft solid,<sup>2,13–15</sup> as well as the forces acting on it. An apparent normal force pulling the solid upwards by the liquid at the contact line is the tension with a magnitude equal to  $\gamma \sin \theta$ ,<sup>16</sup> here  $\gamma$  is the liquid–air surface tension and  $\theta$  is the liquid equilibrium contact angle. A length scale named the elastocapillary length  $\gamma/G$  can be constructed, with the shear modulus  $G$  serving as a resistance to deformation.<sup>15</sup> Earlier computations of the equilibrium shape of the wetting ridge date back to the

studies by Lester<sup>17</sup> and Rusanov,<sup>18</sup> in which a droplet is in contact with a soft semi-infinitely thick substrate. Later, more investigations were done for a soft solid layer of finite thickness  $H$  attached to a rigid substrate.<sup>19,20</sup> All these studies point to a conclusion that both length scales  $\gamma/G$  and  $H$  play a crucial role in solid deformation.

Remarkably, recent studies<sup>15,21–24</sup> have demonstrated that when including the contribution of solid surface tension  $\gamma_s$  to the elastic model, the agreement with the experimentally measured ridge profiles turns out to be promising. The solid surface tension suppresses the deformation and regularizes the singularity at the contact line.<sup>21</sup> The solid angle formed at the contact line follows the balance between the surface forces, or named Neumann's relation.<sup>3,25</sup> Neumann's relation has also been validated by studies using nonlinear elastic constitutive models<sup>26</sup> and experimentally by measurements using confocal microscopy.<sup>9</sup> When  $\gamma/G$  is very small, i.e. rigid solids, one expects the liquid contact angle at the contact line to follow the Young's relation. By including a microscopic length scale  $l_m$  characterizing the width of the liquid–air interface,<sup>27</sup> it is shown that the transition from Neumann's relation to Young's relation occurs when  $\gamma/G \sim l_m$ .<sup>28,29</sup> Young's relation is recovered for  $\gamma/G \ll l_m$ . The crossover from the Neumann's relation to Young's law has also been demonstrated in studies using the molecular dynamics simulations.<sup>30</sup>

Apart from the elastic properties, many soft solids like tissues and gels also demonstrate viscoelastic features. When a droplet is placed in contact with such smooth soft substrates, the flat surface of the solid around the contact line starts to deform and gradually form a wetting ridge. Both experimental<sup>1–6</sup>

Mechanics Division, Department of Mathematics, University of Oslo, 0316 Oslo, Norway. E-mail: [taksc@uio.no](mailto:taksc@uio.no)

† Electronic supplementary information (ESI) available. See DOI: <https://doi.org/10.1039/d2sm00913g>



and theoretical<sup>16</sup> studies find that a sharp tip has developed even at the early stage of ridge formation. Another study<sup>31</sup> investigated the relaxation of a deformed viscoelastic half-space subsequent to the removal of the point load. It was shown that solid surface tension reduces the local elastic deformation and stress field near the load point.

As we mentioned above, the dynamic response of a viscoelastic solid to a time-dependent localized force has been demonstrated by some previous studies. Nevertheless, how different regions of a viscoelastic solid respond in time during the growth and the decay of the ridge has not been fully investigated and described in the literature, in particular the role played by the solid surface tension, which is crucial for the understanding of phenomena such as stick-slip motion of contact lines;<sup>7,32</sup> droplet evaporation<sup>5,33,34</sup> and soft electrowetting.<sup>35</sup> In this study, we examine both the growth and the decay of a ridge and show how the solid interface and the characteristic features of the ridge change with time. Importantly, we focus on the tip region of the ridge and show that the solid material in that region relaxes in a different dynamical way from the remaining part of the ridge. To describe the viscoelastic properties of the soft material, the standard solid model will be implemented. The solutions are computed using the approach of the boundary element method (BEM), which has been used widely to study droplet<sup>36–38</sup> and solid deformation.<sup>39,40</sup> The BEM can be extended to study problems involving viscoelastic deformation coupled with fluid flow such as in wet adhesion.

## 2 Formulation

We consider that a droplet is placed in contact with a layer of isotropic viscoelastic solid with thickness  $H$  which is attached to a rigid solid. We denote the displacement at any position  $\mathbf{x} = x\hat{\mathbf{x}} + y\hat{\mathbf{y}} + z\hat{\mathbf{z}}$  of the undeformed viscoelastic solid and time  $t$  as  $\mathbf{u}(\mathbf{x}, t) = u_x(\mathbf{x}, t)\hat{\mathbf{x}} + u_y(\mathbf{x}, t)\hat{\mathbf{y}} + u_z(\mathbf{x}, t)\hat{\mathbf{z}}$ . In index notations, we write the component as  $u_i$  where  $i = x, y$  or  $z$ . In the following, the subscripts  $i, j$  and  $k$  take either one of the components in rectangular coordinates. The repeated indices conform to the Einstein summation convention, *i.e.*, they are summed over the three components. For viscoelastic materials made of polymers such as elastomers and gels, we assume that the bulk modulus  $K$  can be considered as a constant, independent of time. We further assume that the strain is small, namely the strain tensor  $\varepsilon_{ij}(\mathbf{x}, t) = (\partial u_i/\partial x_j + \partial u_j/\partial x_i)/2 \ll 1$ . Hence, the stress tensor  $\sigma_{ij}(\mathbf{x}, t)$  and the strain tensor follow the linear constitutive relation given as

$$\sigma_{ij}(\mathbf{x}, t) = \int_{-\infty}^t \mathcal{G}(t - \bar{t}; G, G_1, \dots, \eta, \eta_1, \dots) \dot{\varepsilon}_{ij}(\mathbf{x}, \bar{t}) d\bar{t} + K \frac{\partial u_k}{\partial x_k} \delta_{ij}, \quad (1)$$

where the deviatoric part of the strain tensor  $e_{ij} \equiv \varepsilon_{ij} - \varepsilon_{kk} \delta_{ij}/3$ ,  $\dot{\varepsilon}_{ij} \equiv \partial \varepsilon_{ij}/\partial t$  and  $\mathcal{G}$  is the shear relaxation function which depends on the viscoelastic model characterized by the parameters  $G, G_1, \dots$  and  $\eta, \eta_1, \dots$ . We assume the dynamics of the

solid deformation is slow enough so that the net force on a soft solid element vanishes which gives the governing equation

$$\frac{\partial \sigma_{ij}}{\partial x_j} = 0 \quad (2)$$

when body forces such as gravity are neglected.

The range of solid deformation depends on the elastocapillary length  $\gamma/G$  and the thickness of the soft layer  $H$ . In this study, we assume that both the elastocapillary length and the thickness of the soft layer are much smaller than the contact radius  $R$  of the droplet, *i.e.*,  $\gamma/G \ll R$  and  $H \ll R$ , meaning that the solid deformation is localized around the edge of the droplet. In this limit, it is justified to assume that the deformation of a solid behaves as the case of plane strain, for which  $u_x$  and  $u_y$  are a function of  $x$  and  $y$  only, and  $u_z$  is a constant, and so the governing eqn (1) can be simplified due to the conditions of the vanishing of the following quantities, namely

$$\frac{\partial u_z}{\partial z} = \frac{\partial u_x}{\partial x} = \frac{\partial u_y}{\partial y} = \frac{\partial u_x}{\partial z} = \frac{\partial u_y}{\partial z} = 0. \quad (3)$$

In the plane strain situation, the domain of the soft solid layer that we consider is a rectangle with thickness  $H$  and length  $L \gg H$ . Fig. 1 shows the schematic of the setup. The soft layer is attached to a rigid solid, hence at the bottom boundary ( $y = -H$ ) of the domain where the soft and the rigid solids are in contact, the displacement

$$u_i(x, y = -H, t) = 0. \quad (4)$$

At the two other ends of the domain, we also assume the displacements are zero, *i.e.*

$$u_i(x = -L/2, y, t) = u_i(x = L/2, y, t) = 0. \quad (5)$$

The boundary conditions at the solid/fluid interfaces require more discussions. As it has been shown that the solid surface tension plays an important role in the deformation of the wetting ridge, we include this specific property in our model.

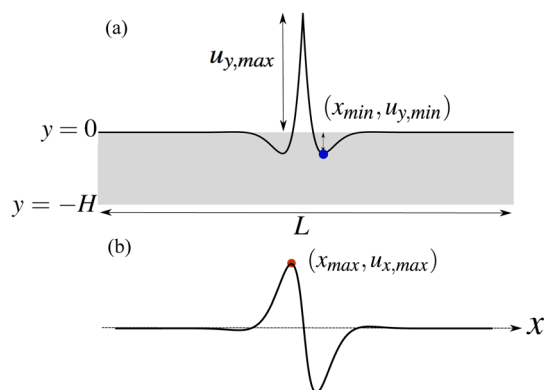


Fig. 1 Schematic of the setup. (a) The gray region represents the undeformed soft layer with a width  $L$  and a thickness  $H$ . The solid curve shows an out-of-plane displacement profile at the solid surface. The maximum is denoted by  $u_{y,max}$  and the local minimum (indicated by a blue circle) is denoted by  $u_{y,min}$  at  $x = x_{min}$ . (b) The solid curve shows an in-plane displacement profile at the solid surface. The maximum (indicated by a red circle) is denoted by  $u_{x,max}$  at  $x = x_{max}$ .



For soft solids, we have to distinguish between surface energy and surface stress due to the Shuttleworth effect.<sup>41–43</sup> In this study, for the simplicity of modelling, we neglect this effect and hence the tension force at the solid interface is independent of the stretching of the solid. We also assume that the surface tensions are the same for the solid/liquid and the solid/air interfaces, hence the tension is described by a constant  $\gamma_s$  along the whole solid interface, and the liquid contact angle  $\theta = 90^\circ$ . We now consider the forces acting on an element of the interface. We first define the traction in the soft solid as  $f_i \equiv \sigma_{ij}n_j$ , where  $n_j$  is the normal vector of a surface pointing outward from an element. We assume that the external force acting on the soft solid only has the out-of-plane component (*i.e.*, the  $y$ -component). Suppose the external force per unit area acting on the interface is given by  $f_i^{\text{ext}}(x, t)$ , for small interface slope due to small deformation  $\partial u_y/\partial x \ll 1$ , we have the force balance on the interface as

$$f_x = -f_x^{\text{ext}} = 0 \quad (6)$$

and

$$f_y + f_y^{\text{ext}} + \gamma_s \frac{\partial^2 u_y}{\partial x^2} = 0, \quad (7)$$

where the normal force balance eqn (7) includes the contribution of the solid surface tension  $\gamma_s$ .<sup>15,22,23</sup> Here we have adopted the approximation for the curvature of the interface, *i.e.*,  $\kappa = \partial^2 u_y/\partial x^2$ , when the slope is small.

To model the localized external traction, we use the Gaussian function to describe the spatial distribution of the normal traction, *i.e.*,  $f_y^{\text{ext}}(x, t) = \Gamma(t) \exp[-x^2/(2\ell_m^2)]/(\ell_m\sqrt{2\pi})$ , where  $\ell_m$  is the microscopic length such that  $\ell_m \ll H$ . In the limit that  $\ell_m \rightarrow 0$ , the traction  $f_y^{\text{ext}}(x, t) = \Gamma(t)\delta(x)$ , where  $\delta(x)$  is the Dirac delta function, which is also used in some other studies.<sup>6</sup> The strength of the external force  $\Gamma(t)$  is a function of time. In this study, we will use two different functional forms, respectively, to investigate the growth and the decay of the ridge, namely case 1:  $\Gamma(t) = \gamma\mathcal{H}(t)$  and case 2:  $\Gamma(t) = \gamma[1 - \mathcal{H}(t)] = \gamma - \gamma\mathcal{H}(t)$ . Here  $\mathcal{H}(t)$  is the Heaviside step function. As the governing equations are linear, the solution for case 2 (decay case) will be obtained by combining the steady solution (at  $t \rightarrow \infty$ ) of case 1 and the solution obtained when using  $\Gamma(t) = -\gamma\mathcal{H}(t)$ .

There are different types of viscoelastic models which have been used to describe the behavior of different viscoelastic materials. The simplest models are the Kelvin–Voigt model or the Maxwell model which consists of a spring and a viscous damper connected in parallel or in series respectively. In this study, we assume the response of the soft material follows the standard solid (Zener) model which consists of a spring (characterized by  $G$ ) connected in parallel with a Maxwell element, *i.e.*, a spring (characterized by  $G_1$ ) connected in series with a viscous damper (characterized by  $\eta$ ), which is relatively simple but can describe both stress relaxation and creep. The standard solid model has been used to describe the viscoelastic behavior of elastomers. We note that our approach can be used for other linear viscoelastic models. Please refer to

the Appendix for the details of the description of the viscoelastic model. Here we point out that for our viscoelastic model, the initial instantaneous shear modulus is  $G + G_1$  and the static (long-term) shear modulus is  $G$ . Since many soft solids can be considered as incompressible, we will take the incompressible limit, *i.e.*  $K \gg (G + G_1)$ .

## 2.1 The boundary element method (BEM)

To solve the governing eqn (1) and (2) with the plane strain conditions (eqn (3)) and the boundary conditions given by eqn (4)–(7), we implement the approach of the boundary element method (BEM) in the time domain.<sup>39,44–46</sup> We denote the closed contour of the boundary of the domain as  $D$ , the position vector of a point on the contour as  $\bar{\mathbf{x}}$  and  $d\bar{l} = \sqrt{d\bar{x}^2 + d\bar{y}^2}$  as the differential length on the contour. The governing eqn (1)–(3) are formulated as boundary integral equations (see the Appendix for the details of derivation) which read

$$\begin{aligned} c(\mathbf{x})u_i(\mathbf{x}, t) &= \int_D \left[ \int_0^t \frac{\partial U_{ij}(\mathbf{x}, \bar{\mathbf{x}}, \bar{t})}{\partial \bar{t}} f_j(\bar{\mathbf{x}}, t - \bar{t}) d\bar{t} + U_{ij}(\mathbf{x}, \bar{\mathbf{x}}, 0) f_j(\bar{\mathbf{x}}, t) \right] d\bar{l}(\bar{\mathbf{x}}) \\ &\quad - \int_D \left[ \int_0^t \frac{\partial P_{ij}(\mathbf{x}, \bar{\mathbf{x}}, \bar{t})}{\partial \bar{t}} u_j(\bar{\mathbf{x}}, t - \bar{t}) d\bar{t} + P_{ij}(\mathbf{x}, \bar{\mathbf{x}}, 0) u_j(\bar{\mathbf{x}}, t) \right] d\bar{l}(\bar{\mathbf{x}}), \end{aligned} \quad (8)$$

where

$$c(\mathbf{x}) = \begin{cases} 1 & \text{for } \mathbf{x} \text{ inside the solid domain} \\ & \text{enclosed by the boundary,} \\ 1/2 & \text{for } \mathbf{x} \text{ on the closed boundary.} \end{cases} \quad (9)$$

The expression of the tensor components  $P_{ij}(\mathbf{x}, \bar{\mathbf{x}}, t)$  and  $U_{ij}(\mathbf{x}, \bar{\mathbf{x}}, t)$  depends on the specific viscoelastic model as for the shear relaxation function  $\mathcal{G}$ . In the Appendix, we derive the expressions for the standard solid (Zener) model. We note that  $P_{ij}$  and  $U_{ij}$  are singular at  $\mathbf{x} = \bar{\mathbf{x}}$ ; the integral over the singular point is thus computed analytically by expanding the tensor components in series around  $\mathbf{x} = \bar{\mathbf{x}}$ .

To solve the boundary integral equations numerically, we implement a time marching scheme<sup>39,44–46</sup> and discretize the boundary of the domain  $D$  as follows: we have evenly distributed marker points for the two side boundaries at  $x = -L/2$  and  $x = L/2$ , and the bottom boundary at  $y = -H$ . The number of marker points, respectively, equals to 50, 50 and 200. For the top boundary at  $y = 0$ , we use 400 marker points and distribute them with a separation increasing exponentially from the center. The distance  $d_m$  between two marker points at the center is as small as  $d_m/H = 10^{-6}$  so that we can resolve the fine structures around the contact line where the localized force is imposed. We take a constant time step  $\delta t$ . At any time  $t = n\delta t$ , the boundary integral eqn (8) is discretized in the



following way (using trapezoidal rule for the time integral):

$$c(\mathbf{x})u_i(\mathbf{x}, n\delta t) = \int_D [U_{ij}(\mathbf{x}, \bar{\mathbf{x}}, 0)f_j(\bar{\mathbf{x}}, n\delta t) + \frac{\delta t}{2}\dot{U}_{ij}(\mathbf{x}, \bar{\mathbf{x}}, 0)f_j(\bar{\mathbf{x}}, n\delta t) - P_{ij}(\mathbf{x}, \bar{\mathbf{x}}, 0)u_j(\bar{\mathbf{x}}, n\delta t) - \frac{\delta t}{2}\dot{P}_{ij}(\mathbf{x}, \bar{\mathbf{x}}, 0)u_j(\bar{\mathbf{x}}, n\delta t) \times (\bar{\mathbf{x}}, n\delta t)]d\bar{\mathbf{x}} + S_i(\mathbf{x}),$$

where  $\dot{U}_{ij}(\mathbf{x}, \bar{\mathbf{x}}, t) = \partial U_{ij}(\mathbf{x}, \bar{\mathbf{x}}, t)/\partial t$ ,  $\dot{P}_{ij}(\mathbf{x}, \bar{\mathbf{x}}, t) = \partial P_{ij}(\mathbf{x}, \bar{\mathbf{x}}, t)/\partial t$  and  $S_i(\mathbf{x})$  is the term corresponding to the history of responses, which can be written as

$$S_i(\mathbf{x}) = \delta t \int_D \sum_{m=1}^{n-1} \dot{U}_{ij}(\mathbf{x}, \bar{\mathbf{x}}, m\delta t)f_j(\bar{\mathbf{x}}, [n-m]\delta t)d\bar{\mathbf{x}} - \delta t \int_D \sum_{m=1}^{n-1} \dot{P}_{ij}(\mathbf{x}, \bar{\mathbf{x}}, m\delta t)u_j(\bar{\mathbf{x}}, [n-m]\delta t)d\bar{\mathbf{x}} + \frac{\delta t}{2} \int_D \dot{U}_{ij}(\mathbf{x}, \bar{\mathbf{x}}, n\delta t)f_j(\bar{\mathbf{x}}, 0) - \dot{P}_{ij}(\mathbf{x}, \bar{\mathbf{x}}, n\delta t)u_j(\bar{\mathbf{x}}, 0)d\bar{\mathbf{x}}. \quad (10)$$

Regarding the rescalings, unless specified differently, we will divide all the lengths by the thickness of the soft layer  $H$ , the stresses by  $\gamma_s/H$  and the time by  $\eta/G$ ; we end up with the following independent dimensionless control parameters (with a tide):

$$\tilde{\gamma} = \frac{\gamma}{\gamma_s}, \tilde{G} = \frac{GH}{\gamma_s}, \tilde{G}_1 = \frac{G_1H}{\gamma_s}, \tilde{t} = \frac{tG}{\eta}, \tilde{\ell}_m = \frac{\ell_m}{H}, \tilde{L} = \frac{L}{H}. \quad (11)$$

## 3 Results

We consider that the width of the soft layer  $L$  is much larger than its thickness  $H$ , and the microscopic length scale  $\ell_m$  is much smaller than the thickness of the soft layer. We take  $\tilde{L} = 50$  and  $\tilde{\ell}_m = 10^{-4}$  (e.g. consider a liquid/air interface of nanometric thickness and a 10 micron thick soft solid layer). We present the results in three main parts. In Section 3.1, we focus on the evolution of the global features of the ridge. In Section 3.2.1, we discuss at how the static solid interface profile depends on the parameters. In Sections 3.2.2 and 3.2.3, the role of the solid surface tension and the relaxation at the tip region is explored in detail.

### 3.1 Shape evolution of the wetting ridge

**3.1.1 Profiles of the wetting ridge during the growth and the decay.** We look at how a wetting ridge grows when  $\tilde{\Gamma}(\tilde{t}) = \tilde{\gamma}\mathcal{H}(\tilde{t})$  and how the ridge decays when  $\tilde{\Gamma}(\tilde{t}) = \tilde{\gamma}[1 - \mathcal{H}(\tilde{t})]$ , with  $\tilde{\gamma} = 0.2$ . As our viscoelastic model is linear, which assumes small solid interfacial slopes (small strains), we thus pick the value of  $\tilde{\gamma}$  to be significantly smaller than 1. Note that the solid interfacial slope around the contact line increases with  $\tilde{\gamma}$  based on the Neumann's relation. The time series of  $\tilde{\Gamma}(\tilde{t})$  is plotted in Fig. 2(a) and (b). We take  $\tilde{G} = 10^{-1}$  and  $\tilde{G}_1 = 10^2$ . Fig. 2(c) and (d) show the out-of-plane displacement  $\tilde{u}_{y0} \equiv \tilde{u}_y(\tilde{x}, \tilde{y} = 0, \tilde{t})$  at

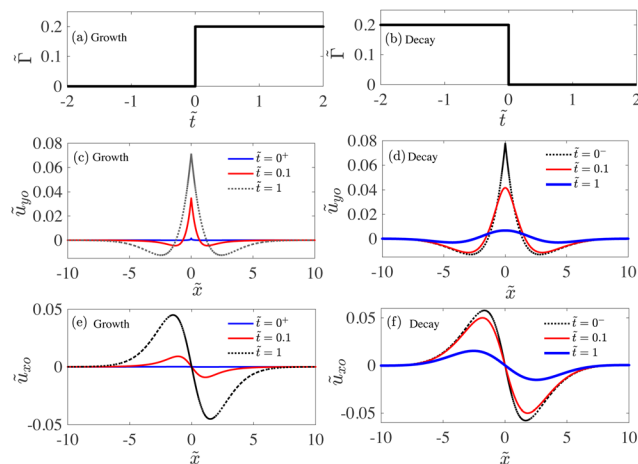


**Fig. 2** (a and b) The time series of the strength of the external stress  $\tilde{\Gamma}(\tilde{t})$ . The growth (c) and (e) and decay (d) and (f) of a wetting ridge. (c and d) The out of plane displacement at the solid–fluid interface  $\tilde{u}_{y0}$  as a function of  $\tilde{x}$  for different rescaled times. (e and f) The in-plane displacement at the solid–liquid interface  $\tilde{u}_{x0}$  as a function of  $\tilde{x}$ . Parameters:  $\tilde{G} = 10^{-1}$ ,  $\tilde{G}_1 = 10^2$ ,  $\tilde{\gamma} = 0.2$ ,  $\tilde{L} = 50$  and  $\tilde{\ell}_m = 10^{-4}$ .

different times. Fig. 2(e) and (f) show the corresponding in-plane displacement  $\tilde{u}_{x0} \equiv \tilde{u}_x(\tilde{x}, \tilde{y} = 0, \tilde{t})$ . At  $\tilde{t} = 0^+$ , there is an instantaneous elastic deformation with shear modulus equal to  $\tilde{G} + \tilde{G}_1$ . As  $\tilde{G}_1$  is large, the initial solid surface deflection is tiny. The ridge shape, described by  $\tilde{u}_{y0}$ , is symmetric along the central axis ( $\tilde{x} = 0$ ) while the in-plane displacement  $\tilde{u}_{x0}$  is anti-symmetric. A significant difference between the growth and the decay of the ridge is that, during the growth, a sharp tip (around  $\tilde{x} = 0$ ) is maintained from the early stage of the growth. For the decay, when the localized external stress vanishes (at  $\tilde{t} = 0$ ), the sharp tip quickly relaxes to round shapes with a much smaller curvature as can be seen in Fig. 2(d). Note that the profiles at  $\tilde{t} = 0^-$  in Fig. 2(d) and (f) are the steady profiles before the external stress vanishes.

**3.1.2 Evolution of the characteristic quantities.** There are several features of the ridge that we can describe here. First, the maximum out-of-plane displacement  $\tilde{u}_{y,\max} \equiv \tilde{u}_{y0}(\tilde{x} = 0, \tilde{t})$  of the solid surface or called the ridge height is at the center  $\tilde{x} = 0$ . Second, the out-of-plane displacement decreases from the center and a minimum value  $\tilde{u}_{y,\min} \equiv \tilde{u}_{y0}(\tilde{x} = \tilde{x}_{\min}, \tilde{t})$  is achieved at  $\tilde{x} = \tilde{x}_{\min}$  (and  $\tilde{x} = -\tilde{x}_{\min}$ ), where a clear dimple is formed with a negative out-of-plane displacement. Third, for the in-plane displacement  $\tilde{u}_{x0}$ , we see from Fig. 2(e) and (f) that around the center  $\tilde{x} = 0$ , the solid material is compressed (with a negative slope shown in the plot, i.e.,  $\partial \tilde{u}_{x0}/\partial \tilde{x} < 0$ ), and there is a maximum  $\tilde{u}_{x,\max} \equiv \tilde{u}_{x0}(\tilde{x} = \tilde{x}_{\max}, \tilde{t})$  at the negative side of  $\tilde{x}$ . These characteristic quantities are also indicated in the schematic of the setup in Fig. 1.

Now we look at the evolution of the characteristic quantities. In Fig. 3(a) and (b), we plot  $\tilde{u}_{y,\max}$ ,  $|\tilde{u}_{y,\min}|$  and  $\tilde{u}_{x,\max}$  as a function of the rescaled time  $\tilde{t}$ , respectively, during the growth and the decay of the ridge. All these quantities increase/decrease monotonically with time and saturate to a steady value during the growth/decay of the ridge. Next, we look at



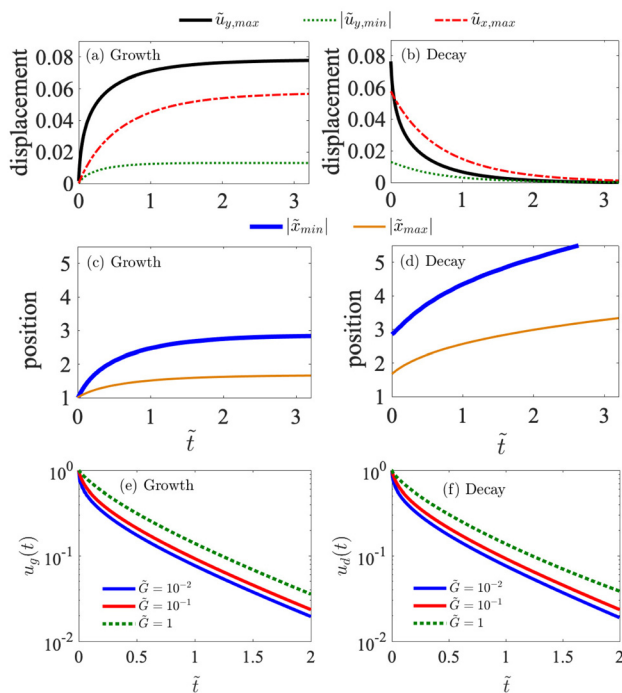


**Fig. 3** (a and b) The rescaled ridge height  $\tilde{u}_{y,\max}$ , the absolute value of the rescaled minimum out-of-plane displacement  $|\tilde{u}_{y,\min}|$  and the rescaled maximum in-plane displacement  $\tilde{u}_{x,\max}$  as a function of the rescaled time  $\tilde{t}$ . (c and d) The absolute value of  $\tilde{x}_{\min}$  and  $\tilde{x}_{\max}$  as a function of the rescaled time  $\tilde{t}$ . For (a–d),  $\tilde{G} = 10^{-1}$ . (e and f) The rescaled ridge height  $\tilde{u}_g$  in (e) and  $\tilde{u}_d$  in (f) as a function of the rescaled time  $\tilde{t}$  for different values of  $\tilde{G}$ . Parameters:  $\tilde{G}_1 = 10^2$ ,  $\tilde{\gamma} = 0.2$ ,  $\tilde{L} = 50$  and  $\tilde{\ell}_m = 10^{-4}$ .

the time series of the magnitudes of the positions  $|\tilde{x}_{\min}|$  and  $|\tilde{x}_{\max}|$  as plotted in Fig. 3(c) and (d). Both  $|\tilde{x}_{\min}|$  and  $|\tilde{x}_{\max}|$  equal to unity at  $\tilde{t} = 0^+$  (instantaneous elastic response). This means that for a large  $\tilde{G}_1$ , these two positions are equal to the thickness of the soft substrate. They increase with time during the growth. However, during the decay of the ridge, instead of decreasing, the positions still increase with time. This feature can also be observed from the profiles shown in Fig. 2(d) and (f).

To characterize the dynamics of the whole wetting ridge, we here focus on the evolution of the ridge height  $\tilde{u}_{y,\max}$ . For both the growth and the decay, we find that, a rescaled ridge height relaxes exponentially to the steady states at late times.

The rescaled ridge heights are defined as  $\tilde{u}_g(\tilde{t}) \equiv$

$$\frac{\tilde{u}_{y,\max}(\tilde{t} \rightarrow \infty) - \tilde{u}_{y,\max}(\tilde{t})}{\tilde{u}_{y,\max}(\tilde{t} \rightarrow \infty) - \tilde{u}_{y,\max}(\tilde{t} = 0^+)}$$

$$\text{for the growth and } \tilde{u}_d(\tilde{t}) \equiv \frac{\tilde{u}_{y,\max}(\tilde{t})}{\tilde{u}_{y,\max}(\tilde{t} = 0^+)}$$

for the decay. In Fig. 3(e) and (f), the rescaled ridge heights are respectively plotted as a function of  $\tilde{t}$  for different values of  $\tilde{G}$ . We find that both  $\tilde{u}_g(\tilde{t})$  and  $\tilde{u}_d(\tilde{t})$  relax the same way, *i.e.*,  $\tilde{u}_g(\tilde{t})$  or  $\tilde{u}_d(\tilde{t})$ , scales as  $\sim \exp(-1.15\tilde{t})$  at late times. The late time ridge evolution possesses the same time scale as the relaxation of the viscoelastic material in our standard solid model, *i.e.*,  $\eta/G$ .

## 3.2 The role of the solid surface tension

### 3.2.1 Static profiles: from the soft regime to the stiff regime.

Before we look at the dynamic response of the soft solid at the tip region of the ridge, it is insightful to see how the static shape (purely elastic) of solid deformation at the tip region varies when  $\tilde{G}$  is changed. Note that the static shape is the same as the shape at  $\tilde{t} \rightarrow \infty$  in the growth case. From the scaling with  $\tilde{G}$ , we will also deduce the dependence on the shear modulus  $G$  and the soft layer thickness  $H$ , which are dimensional quantities of physical and practical importance. Before we focus on the tip region, let us first look at the ridge height  $\tilde{u}_{y,\max}(\tilde{t} \rightarrow \infty)$ , which is plotted in Fig. 4(a) as a function of  $\tilde{G}$ . As one might expect, the ridge height increases with decreasing  $\tilde{G}$ . Moreover, when  $\tilde{G} \gg 1$  or in other words, when the soft layer thickness is much larger than the elastocapillary length  $\gamma_s/G$ , we

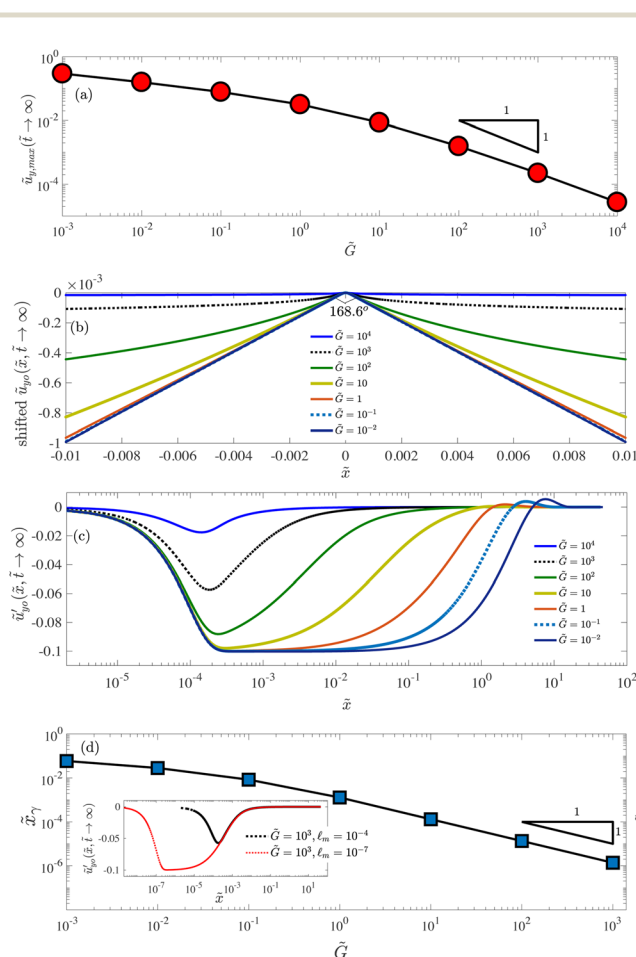


**Fig. 4** Static states: solutions for the growth case when  $\tilde{t} \rightarrow \infty$ . (a) The static ridge height  $\tilde{u}_{y,\max}(\tilde{t} \rightarrow \infty)$  as a function of  $\tilde{G}$ . (b) The static solid interface profile  $\tilde{u}_{y_0}(\tilde{x}, \tilde{t} \rightarrow \infty)$  shifted by the static ridge height as a function of  $\tilde{x}$  for a wide range of  $\tilde{G}$ . (c) The slope of the static solid interface  $\tilde{u}'_{y_0}(\tilde{x}, \tilde{t} \rightarrow \infty)$  vs.  $\tilde{x}$ . (d) The size of the constant-slope region  $\tilde{x}_\gamma$  as a function of  $\tilde{G}$ . Here  $\tilde{\ell}_m = 10^{-7}$ , we increase the numerical resolution around the contact line by having the smallest separation of marker points  $\approx 10^{-9}$ . Inset: The slope of the static solid interface  $\tilde{u}'_{y_0}(\tilde{x}, \tilde{t} \rightarrow \infty)$  vs.  $\tilde{x}$  for  $\tilde{\ell}_m = 10^{-4}$  and  $\tilde{\ell}_m = 10^{-7}$  and a fixed value of  $\tilde{G} = 10^3$ . Parameters:  $\tilde{\gamma} = 0.2$ ,  $\tilde{L} = 50$ , and  $\tilde{\ell}_m = 10^{-4}$  for (a–c).



find that  $\tilde{u}_{y,\max}(\tilde{t} \rightarrow \infty) \sim \tilde{G}^{-1}$ . This scaling implies that the dimensional ridge height  $u_{y,\max}(\tilde{t} \rightarrow \infty)$  scales linearly with the elastocapillary length and is independent of the soft layer thickness. The confinement (thickness) of the soft layer plays no role in this regime. When  $\tilde{G}$  becomes smaller ( $\lesssim 10$ ), we see that  $\tilde{u}_{y,\max}(\tilde{t} \rightarrow \infty)$  scales as  $\tilde{G}^\alpha$  locally with  $-1 < \alpha < 0$ . Hence  $u_{y,\max}(\tilde{t} \rightarrow \infty)$  increases with decreasing  $G$  and increasing  $H$ .

In the following, we focus on the tip region. In Fig. 4(b), we plot the static out-of-plane displacement  $\tilde{u}_{y0}(\tilde{x}, \tilde{t} \rightarrow \infty)$  in the region of  $-0.01 < \tilde{x} < 0.01$ , for a wide range of  $\tilde{G} = 10^{-2}$ – $10^4$ . Note that the profiles are shifted by the ridge height  $\tilde{u}_{y,\max}(\tilde{t} \rightarrow \infty)$  so that all the tips are at the same position. For  $\tilde{G} \leq 10$ , we see the solid interfaces form the same solid angle  $\theta_s = 168.6^\circ$ . The solid angle can be understood by the force balance between the solid surface tensions and the external liquid–air surface tension, namely  $\gamma = 2\gamma_s \cos(\theta_s/2)$ . For  $\tilde{G} > 10$ , the interface profiles have a solid angle getting closer to  $180^\circ$  as  $\tilde{G}$  increases. This shows how the solid deformation at the tip region varies from a soft regime to a stiff regime which are consistent with Neumann's relation and Young's relation, respectively, in the two different limits.

To show clearly how the slope of the solid interface varies with the distance from the center at different length scales, we plot the interfacial slope  $\tilde{u}'_{y0}(\tilde{x}, \tilde{t} \rightarrow \infty) \equiv \partial \tilde{u}_{y0}(\tilde{x}, \tilde{t} \rightarrow \infty) / \partial \tilde{x}$  as a function of  $\tilde{x}$  (in log scale) in Fig. 4(c). For the stiffer case we have computed here, e.g.  $\tilde{G} = 10^4$ , the magnitude of the slope is small. The whole solid interface maintains close to a flat surface even though being exerted by a localized external force. As  $\tilde{G}$  decreases, the magnitude of the slope increases. There appear overlapping regions of the curves for different  $\tilde{G}$  values. The size of the overlapping region increases with decreasing  $\tilde{G}$ . The overlapping of the curves means that the solid deformation in that region is independent of  $\tilde{G}$ , and hence the solid surface tension dominates over the elastic stress. Moreover, we also see that there is a region of a constant slope  $-0.1$  for  $\tilde{G} < 10$ . Note that the slope  $-0.1$  means that the solid angle  $\theta_s = 168.6^\circ$ . Indeed the constant-slope region is what we have plotted in Fig. 4(b). At distances from the center  $\tilde{x}$  smaller than  $\tilde{\ell}_m = 10^{-4}$ , the distribution of external stress plays a role, the slope of the interface is not  $-0.1$ , although the solid surface tension dominates over the elastic stress (for  $\tilde{G} \leq 10$ ). It is important to point out that  $\tilde{\ell}_m$  plays a role for the existence of a region where Neumann's relation is valid. When taking  $\tilde{\ell}_m \rightarrow 0$ , there always exists a region close enough to  $\tilde{x} = 0$  where the Neumann's relation is valid for any  $\tilde{G}$  values. For example, in the inset of Fig. 4(d), we plot  $\tilde{u}'_{y0}(\tilde{x}, \tilde{t} \rightarrow \infty)$  as a function of  $\tilde{x}$  for both  $\tilde{\ell}_m = 10^{-4}$  and  $\tilde{\ell}_m = 10^{-7}$ , and a fixed value of  $\tilde{G} = 10^3$ . We find that when approaching the contact line ( $\tilde{x} = 0$ ) from a large distance, the curves of  $\tilde{u}'_{y0}(\tilde{x}, \tilde{t} \rightarrow \infty)$  for  $\tilde{\ell}_m = 10^{-4}$  and  $\tilde{\ell}_m = 10^{-7}$  overlap until  $\tilde{x} \approx 3 \times 10^{-4}$  where  $\tilde{\ell}_m$  starts to play a role. In the case of  $\tilde{\ell}_m = 10^{-7}$ , the magnitude of the interfacial slope keeps increasing until  $\tilde{x} \approx 3 \times 10^{-7}$  for which  $\tilde{u}'_{y0}(\tilde{x} \approx 3 \times 10^{-7}, \tilde{t} \rightarrow \infty) \approx -0.1$  and a constant-slope region is observed around  $\tilde{x} \approx 3 \times 10^{-7}$ . In reality, the thickness of the interface (i.e.  $\ell_m$ ) is in the nanometric

scales, that means when  $\tilde{G}$  is larger than a certain value, Neumann's relation cannot be observed at any distance from the contact line. Instead, the solid interface maintains as a flat surface as we have shown in Fig. 4(b) and (c).

How does the size of the constant-slope region depend on  $\tilde{G}$ ? To address this issue, we introduce the boundary of the constant-slope region as follows. We define  $\tilde{x}_\gamma$  as the largest value of  $|\tilde{x}|$  such that  $|\tilde{u}'_{y0}(|\tilde{x}| = \tilde{x}_\gamma)| = 0.099$ . Thus when  $3\tilde{\ell}_m \approx |\tilde{x}| < \tilde{x}_\gamma$ , we have  $|\tilde{u}'_{y0}(\tilde{x})| \approx 0.1$ , which defines the range of the constant-slope region. Since the constant-slope-region disappears for large  $\tilde{G}$  when  $\tilde{\ell}_m$  is not small enough, we here use  $\tilde{\ell}_m = 10^{-7}$  in our computations. In Fig. 4(d), we plot  $\tilde{x}_\gamma$  as a function of  $\tilde{G}$ . As we have demonstrated already in Fig. 4(c), we find that  $\tilde{x}_\gamma$  increases with decreasing  $\tilde{G}$ . Similar to the scaling of the ridge height, when  $\tilde{G} \gg 1$ , the size of the constant-slope region  $\tilde{x}_\gamma \sim \tilde{G}^{-1}$ , which implies that the dimensional quantity  $x_\gamma$  scales linearly with the elastocapillary length  $\gamma_s/G$  and is independent of the soft layer thickness. When  $\tilde{G} \lesssim 1$ , we see that  $\tilde{x}_\gamma$  scales as  $\tilde{G}^\beta$  locally with  $-1 < \beta < 0$ . Hence the dimensional size  $x_\gamma$  increases with decreasing  $G$  and increasing  $H$ . We end this section with an example to estimate the dimensional size of the constant-slope region. Taking the shear modulus  $G = 1$  kPa, the thickness of the soft layer  $H = 10$   $\mu\text{m}$ , the solid surface tension  $\gamma_s = 0.01$   $\text{N m}^{-1}$  and  $\gamma = 0.002$   $\text{N m}^{-1}$ , we get  $\tilde{G} = 1$ . From Fig. 4(d), we obtain  $\tilde{x}_\gamma \approx 10^{-3}$ , i.e.,  $x_\gamma \approx 10$  nm. No constant-slope-region can be observed when  $x_\gamma \lesssim 3\ell_m$ .

**3.2.2 Dynamic response at the tip region during the growth.** We first look at the growth case. We take  $\tilde{G} = 10^{-1}$  and  $\tilde{G}_1 = 10^2$ . In Fig. 5(a), the interfacial slope  $\tilde{u}'_{y0}(\tilde{x}, \tilde{t}) \equiv \partial \tilde{u}_{y0}(\tilde{x}, \tilde{t}) / \partial \tilde{x}$  as a function of  $\tilde{x}$  (in log scale) is plotted for different times. At  $\tilde{t} = 0^+$ , the solid responds by an instantaneous elastic deformation. As time goes on, we observe that there is a region around the tip where the interfacial slope is independent of the time after. The size of this region grows with time. For example, this region has a range  $0 < \tilde{x} \lesssim 10^{-4}$  at  $\tilde{t} = 0^+$  and  $0 < \tilde{x} \lesssim 10^{-3}$  at  $\tilde{t} = 0.02$ . To understand this result, we note that the shear modulus relaxes from  $\tilde{G} + \tilde{G}_1$  to  $\tilde{G}$  for our viscoelastic model. We have also shown in Fig. 4(c) and (d) that there exists a surface-tension-dominated region with a size increasing with decreasing  $\tilde{G}$ . Hence, once a solid element relaxes to within the surface-tension-dominated region, the solid element is in an equilibrium state. The time taken to relax to an equilibrium state thus depends on the distance from the center. The solid relaxes to an equilibrium state in a shorter time for materials closer to the center as we have shown in Fig. 5(a). In contrast, for stiffer solid materials for which no surface-tension-dominated region exists, all the solid elements relax in the same time scale  $\eta/G$  as shown in one example in Fig. 5(b) in which  $\tilde{G} = 10^3$  and  $\tilde{G}_1 = 10^4$ .

How does the relaxation at the tip region depend on material parameters? To address this question, we pick a position  $\tilde{x} = \tilde{x}_0 = 10^{-2}$  and study how the solid interface slope at this position varies with time for different values of  $\tilde{G}$ ,  $\tilde{G}_1$  and  $\tilde{\gamma}$ . We find that the slope relaxation is independent of  $\tilde{G}$  when plotting



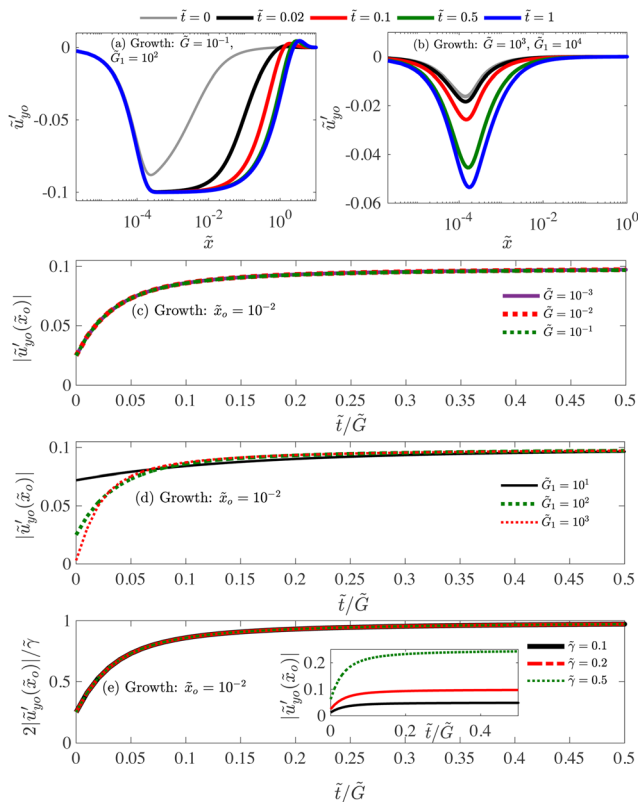


**Fig. 5** The slope of solid interface  $\tilde{u}'_{y_0}$  vs.  $\tilde{x}$  for different rescaled times  $\tilde{t}$  during the growth of the ridge for  $\tilde{G} = 10^{-1}$ ,  $\tilde{G}_1 = 10^2$  in (a) and for  $\tilde{G} = 10^3$ ,  $\tilde{G}_1 = 10^4$  in (b). Other parameters:  $\tilde{\gamma} = 0.2$ ,  $\tilde{L} = 50$  and  $\tilde{\ell}_m = 10^{-4}$ . (c and d) The slope  $|\tilde{u}'_{y_0}(\tilde{x} = \tilde{x}_0, \tilde{t})|$  as a function of the rescaled time  $\tilde{t}/\tilde{G}$ . Here  $\tilde{x}_0 = 10^{-2}$ . Other parameters:  $\tilde{\gamma} = 0.2$ ,  $\tilde{G}_1 = 10^2$  for (c) and  $\tilde{G} = 10^{-2}$  for (d). (e) The slope  $|\tilde{u}'_{y_0}(\tilde{x} = \tilde{x}_0, \tilde{t})|$  rescaled by  $\tilde{\gamma}/2$  as a function of the rescaled time  $\tilde{t}/\tilde{G}$  for different  $\tilde{\gamma}$ . Inset: The slope  $|\tilde{u}'_{y_0}(\tilde{x} = \tilde{x}_0, \tilde{t})|$  vs.  $\tilde{t}/\tilde{G}$  for different  $\tilde{\gamma}$ . Other parameters:  $\tilde{G} = 10^{-1}$  and  $\tilde{G}_1 = 10^2$ .

$|\tilde{u}'_{y_0}(\tilde{x} = \tilde{x}_0, \tilde{t})|$  as a function of the rescaled time  $\tilde{t}/\tilde{G}$  as shown in Fig. 5(c). In other words, the relaxation at the tip region is much shorter than the long-term relaxation of the ridge. Note that  $\tilde{t}/\tilde{G} = \tau\gamma_s/\eta H$ . On the other hand, the short-term shear modulus  $\tilde{G}_1$  does play a role as shown in Fig. 5(d). It is interesting to see how the surface tensions determine the tip relaxation. In Fig. 5(e), we plot  $|\tilde{u}'_{y_0}(\tilde{x} = \tilde{x}_0, \tilde{t})|$  recalled by  $\tilde{\gamma}/2$  as a function of  $\tilde{t}/\tilde{G}$  for different values of  $\tilde{\gamma}$ ; all curves collapse on each other. Hence we find that  $|\tilde{u}'_{y_0}(\tilde{x} = \tilde{x}_0, \tilde{t})|$  scales linearly with  $\tilde{\gamma}$ . From the results we have shown, the relaxation of the slope can be written as  $|\tilde{u}'_{y_0}(\tilde{x} = \tilde{x}_0, \tilde{t})| = (\gamma/\gamma_s)F(\tau\gamma_s/\eta H, \tilde{G}_1, \tilde{x}_0)$ , with the functional form of  $F$  undetermined. The physical interpretation is as follows: the ratio  $\gamma/\gamma_s$  determines the equilibrium slope (solid angle). The relaxation time scale is determined by the solid surface tension  $\gamma_s$  and the short-term relaxation time of the viscoelastic material. The relaxation is characterized by a spreading velocity  $\gamma_s/\eta$ .

### 3.2.3 Dynamic response at the tip region during the decay.

Once the external force disappears, the sharp tip relaxes immediately. How does the tip region relax during the decay

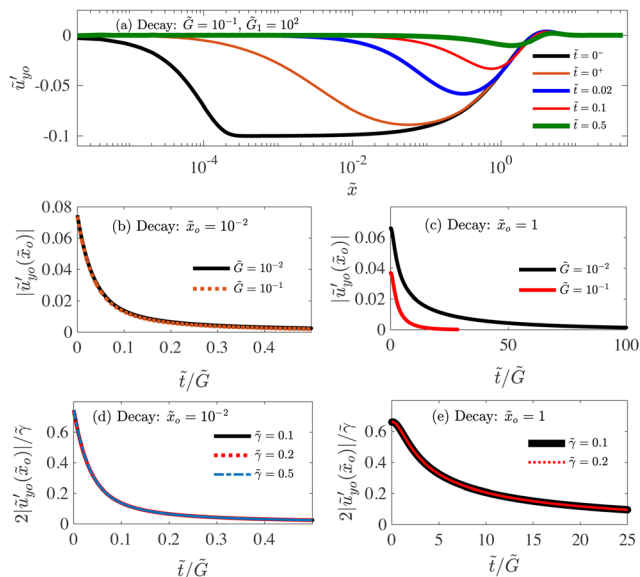


**Fig. 6** (a) The slope of solid interface  $\tilde{u}'_{y_0}$  vs.  $\tilde{x}$  for different rescaled times  $\tilde{t}$  during the decay of the ridge for  $\tilde{G} = 10^{-1}$  and  $\tilde{G}_1 = 10^2$ . Other parameters:  $\tilde{\gamma} = 0.2$ ,  $\tilde{L} = 50$  and  $\tilde{\ell}_m = 10^{-4}$ . (b and c) The magnitude of the slope  $|\tilde{u}'_{y_0}(\tilde{x} = \tilde{x}_0, \tilde{t})|$  as a function of the rescaled time  $\tilde{t}/\tilde{G}$ . Here  $\tilde{x}_0 = 10^{-2}$  in (b) and  $\tilde{x}_0 = 1$  in (c). Other parameters:  $\tilde{G}_1 = 10^2$  and  $\tilde{\gamma} = 0.2$ . (d and e) The slope  $|\tilde{u}'_{y_0}(\tilde{x} = \tilde{x}_0, \tilde{t})|$  rescaled by  $\tilde{\gamma}/2$  as a function of the rescaled time  $\tilde{t}/\tilde{G}$  for different  $\tilde{\gamma}$ . Here  $\tilde{x}_0 = 10^{-2}$  in (d) and  $\tilde{x}_0 = 1$  in (e). Other parameters:  $\tilde{G} = 10^{-2}$  and  $\tilde{G}_1 = 10^2$ .

of the ridge? In Fig. 6(a), we show the slope  $|\tilde{u}'_{y_0}(\tilde{x}, \tilde{t})|$  as a function of  $\tilde{x}$  (in log scale) for different times during the decay. As there is an instantaneous elastic response at  $\tilde{t} = 0^+$ , the constant-slope-region may disappear as early as at  $\tilde{t} = 0^+$  as shown in Fig. 6(a) for which  $\tilde{G}_1 = 10^2$ . Since the static shape at the tip region is determined by the surface tensions (in the soft regime), one may expect the tip region relaxes differently from the rest part of the ridge during the decay, as we have observed for the growth case. To address this question, we pick two positions, *i.e.*  $\tilde{x} = \tilde{x}_0 = 10^{-2}$  and  $\tilde{x} = \tilde{x}_0 = 1$ , and study how the solid interface slope  $|\tilde{u}'_{y_0}(\tilde{x} = \tilde{x}_0, \tilde{t})|$  at these two positions varies with time for two different values of  $\tilde{G}$ , namely  $\tilde{G} = 10^{-1}$  and  $\tilde{G} = 10^{-2}$ . Note that from Fig. 4(d),  $\tilde{x}_0 = 10^{-2} \lesssim \tilde{x}$ , and  $\tilde{x}_0 = 1 \gg \tilde{x}$ . In Fig. 6(b), we see that at  $\tilde{x}_0 = 10^{-2}$ , the evolution of the interfacial slope is the same for  $\tilde{G} = 10^{-1}$  and  $\tilde{G} = 10^{-2}$ . However, at  $\tilde{x}_0 = 1$ , the slope evolves differently as we can see in Fig. 6(c), and the time scale depends on  $\eta/G$ , which is much larger than the relaxation time at the tip region. On the other hand, the slope scales with  $\tilde{\gamma}$  for both  $\tilde{x} = \tilde{x}_0 = 10^{-2}$  and  $\tilde{x} = \tilde{x}_0 = 1$  as we have shown in Fig. 6(d) and (e), in which the y-axis is  $|\tilde{u}'_{y_0}(\tilde{x} = \tilde{x}_0, \tilde{t})|$  rescaled by  $\tilde{\gamma}/2$ . This is because the out-of-plane displacement depends linearly with  $\gamma$  for the whole ridge, and hence the ratio  $\gamma/\gamma_s$  determines the interfacial slope.

## 4 Discussion and conclusions

In summary, we study the dynamic response of an incompressible viscoelastic solid being acted upon by a localized surface



force. The responses of the global features of the wetting ridge, *e.g.*, the growth and the decay of the ridge height, depend on the rheological properties of the solid material. For the standard solid model we implement in this study, the ridge height relaxes exponentially at late time with a time scale given by  $\eta/G$ . Some other studies use the Chasset-Thirion model to describe the viscoelastic behavior of silicone gels;<sup>6</sup> the relaxation of the ridge is found to follow a power law with time. The dynamic around the tip, on the other hand, is different from the remaining part of the soft solid during both the growth and the decay. For the growth, the equilibrium state of a solid element is achieved when it is within the surface-tension-dominated region, which has a size increasing with time due to viscoelastic properties of the solid. Hence an equilibrium can be achieved within a time scale much shorter than the relaxation time of the shear modulus of the viscoelastic material ( $\eta/G$ ). Similarly for the decay, the tip region relaxes with time scales that depend significantly on the solid surface tension, namely the relaxation has a characteristic spreading velocity  $\gamma_s/\eta$ . Although the results presented in this study are obtained using the standard solid model, the existence of the surface-tension-dominated region at the ridge tip is expected to be universal. Hence the features of the dynamics at the tip region shown in this study can be compared with experimental measurements given that the viscoelastic properties of the solid material are determined.

How does the dynamic response of a soft solid play a role when a droplet is in motion? Current models<sup>4,6,47</sup> assume dissipation being dominated by the viscoelastic effects in the soft solid and neglect flow in the fluids, and consider a constant contact line velocity. On the other hand, experimental studies observe the stick-slip motion of the contact line.<sup>7</sup> The interplay between the fluid flow and the time-dependent morphological changes of the wetting ridge is expected to be crucial for the dynamics of the contact line and the droplet motion, which remains a challenging topic to be explored. Our findings show the features of the local morphological changes at the ridge tip during both growth and relaxation, which provide an important fundamental knowledge for investigating a contact line moving over a soft surface.

## Conflicts of interest

There are no conflicts to declare.

## Appendix A1. Derivation of the boundary integral equation in time domain for linear viscoelastic models (plane strain cases)

We here decompose the stress  $\sigma_{ij}(\mathbf{x}, t)$  and the strain  $\varepsilon_{ij}(\mathbf{x}, t)$  tensors into the hydrostatic and deviatoric parts. Namely, we write

$$\sigma_{ij} = \frac{\sigma_{kk}}{3} \delta_{ij} + s_{ij} \quad (12)$$

and

$$\varepsilon_{ij} = \frac{\varepsilon_{kk}}{3} \delta_{ij} + e_{ij}, \quad (13)$$

with the strain tensor defined as

$$\varepsilon_{ij} = \frac{1}{2} \left( \frac{\partial u_i}{\partial x_j} + \frac{\partial u_j}{\partial x_i} \right). \quad (14)$$

For isotropic linear viscoelastic materials, the constitutive relations can be written in the generalized differential forms which read

$$\sum_{l=0}^l p_l \frac{\partial^l s_{ij}}{\partial t^l} = \sum_{m=0}^m q_m \frac{\partial^m e_{ij}}{\partial t^m}, \quad (15)$$

and

$$\sum_{l=0}^l a_l \frac{\partial^l \sigma_{kk}}{\partial t^l} = \sum_{m=0}^m b_m \frac{\partial^m \varepsilon_{kk}}{\partial t^m}, \quad (16)$$

where  $p_l$ ,  $q_m$ ,  $a_l$  and  $b_m$  are coefficients that depend on the specific viscoelastic model. Applying Laplace transform to the constitutive relations (15) and (16), with Laplace transform of a function  $f(t)$  defined as  $\mathcal{L}[f(t)] \equiv \int_0^\infty f(t) \exp(-st) dt$ , the constitutive relation can be written as<sup>44</sup>

$$\Sigma_{ij}(\mathbf{x}, s) = \hat{K}(s) E_{kk}(\mathbf{x}, s) \delta_{ij} + 2\hat{G}(s) E_{ij}(\mathbf{x}, s), \quad (17)$$

where  $\Sigma_{ij}(\mathbf{x}, s) \equiv \mathcal{L}[\sigma_{ij}(\mathbf{x}, t)]$ ,  $E_{kk}(\mathbf{x}, s) \equiv \mathcal{L}[\varepsilon_{kk}(\mathbf{x}, t)]$  and  $E_{ij}(\mathbf{x}, s) \equiv \mathcal{L}[e_{ij}(\mathbf{x}, t)]$ . The expressions in Laplace space of the bulk modulus  $\hat{K}(s) = \left( \sum_{k=0}^j b_k s^k \right) / \left( 3 \sum_{l=0}^i a_l s^l \right)$  and the shear modulus  $\hat{G}(s) = \left( \sum_{k=0}^j q_k s^k \right) / \left( 2 \sum_{l=0}^i p_l s^l \right)$ . In Appendix A2 we show how to obtain them for the standard solid (Zener) model. Eqn (17) has the same form as the linear elastic constitutive relation. Hence by following the same approach of deriving the boundary integral equation for a purely linear elastic material in the quasi-static state ( $\partial\sigma_{ij}/\partial x_j = 0$ ), we can obtain the boundary integral equations for linear viscoelastic models in the Laplace space. Here we consider plane strain cases, for which the boundary integral equation in Laplace space is given as<sup>45</sup>

$$c(\mathbf{x}) \hat{u}_i(\mathbf{x}, s) = \int_D s \hat{U}_{ij}(\mathbf{x}, \bar{\mathbf{x}}, s) \hat{f}_j(\bar{\mathbf{x}}, s) dl(\bar{\mathbf{x}}) - \int_D s \hat{P}_{ij}(\mathbf{x}, \bar{\mathbf{x}}, s) \hat{u}_j(\bar{\mathbf{x}}, s) dl(\bar{\mathbf{x}}) \quad (18)$$

where

$$c(\mathbf{x}) = \begin{cases} 1 & \text{for } \mathbf{x} \text{ inside the solid domain} \\ & \text{enclosed by the boundary,} \\ 1/2 & \text{for } \mathbf{x} \text{ on the closed boundary,} \end{cases} \quad (19)$$

$\hat{u}_j(\mathbf{x}, s) \equiv \mathcal{L}[u_j(\mathbf{x}, t)]$ ,  $\hat{f}_j(\mathbf{x}, s) \equiv \mathcal{L}[\sigma_{ij}(\mathbf{x}, t) n_j(\mathbf{x})]$ , with  $\mathbf{n}$  being the normal vector pointing outward the soft solid domain, and the line integrals on the right hand side are carried out along the closed contour  $D$  of the boundary of the domain with  $dl(\bar{\mathbf{x}})$



denoting the differential length of  $D$  and  $\bar{\mathbf{x}} = \bar{x}\hat{\mathbf{x}} + \bar{y}\hat{\mathbf{y}}$  being the position vector of a point on the contour. The functions  $\hat{U}_{ij}(\mathbf{x}, \bar{\mathbf{x}}, s)$  and  $\hat{P}_{ij}(\mathbf{x}, \bar{\mathbf{x}}, s)$  are given by<sup>45,46</sup>

$$\hat{U}_{ij}(\mathbf{x}, \bar{\mathbf{x}}, s) = \frac{1}{8\pi} \left[ \hat{J}_1(s) \delta_{ij} \log\left(\frac{1}{r}\right) + \hat{J}_2(s) r_i r_j \right], \quad (20)$$

$$\hat{P}_{ij}(\mathbf{x}, \bar{\mathbf{x}}, s) = \frac{1}{8\pi r} \left\{ \hat{J}_3(s) \left( r_i n_j - r_j n_i - \frac{\partial r}{\partial n} \delta_{ij} \right) + \hat{J}_4(s) \left[ \frac{\partial r}{\partial n} (\delta_{ij} - 4r_i r_j) + r_j n_i - r_i n_j \right] \right\}, \quad (21)$$

where  $r = [(x - \bar{x})^2 + (y - \bar{y})^2]^{1/2}$ ,  $r_x = \frac{\partial r}{\partial x} = (\bar{x} - x)/r$ ,  $r_y = \frac{\partial r}{\partial y} = (\bar{y} - y)/r$  and  $\frac{\partial r}{\partial n} = n_x \frac{\partial r}{\partial x} + n_y \frac{\partial r}{\partial y}$ . The functions  $\hat{J}_1(s)$ ,  $\hat{J}_2(s)$ ,  $\hat{J}_3(s)$  and  $\hat{J}_4(s)$  are given as

$$\hat{J}_1(s) = \frac{2[3\hat{K}(s) + 7\hat{G}(s)]}{s\hat{G}(s)[3\hat{K}(s) + 4\hat{G}(s)]}, \quad \hat{J}_2(s) = \frac{2[3\hat{K}(s) + \hat{G}(s)]}{s\hat{G}(s)[3\hat{K}(s) + 4\hat{G}(s)]},$$

$$\hat{J}_3(s) = \frac{2[3\hat{K}(s) + 7\hat{G}(s)]}{s[3\hat{K}(s) + 4\hat{G}(s)]}, \quad \hat{J}_4(s) = \frac{2[3\hat{K}(s) + \hat{G}(s)]}{s[3\hat{K}(s) + 4\hat{G}(s)]}. \quad (22)$$

To obtain the boundary integral equation in the time domain,<sup>39,44-46</sup> we perform an inverse Laplace transform  $\mathcal{L}^{-1}$  to eqn (18) and obtain

$$c(\mathbf{x})u_i(\mathbf{x}, \mathbf{t}) = \int_D \mathcal{L}^{-1} \left[ s \hat{U}_{ij}(\mathbf{x}, \bar{\mathbf{x}}, s) \hat{f}_j(\bar{\mathbf{x}}, s) \right] d\mathbf{l}(\bar{\mathbf{x}}) - \int_D \mathcal{L}^{-1} \left[ s \hat{P}_{ij}(\mathbf{x}, \bar{\mathbf{x}}, s) \hat{u}_j(\bar{\mathbf{x}}, s) \right] d\mathbf{l}(\bar{\mathbf{x}}) = \int_D \left[ \int_0^t \frac{\partial U_{ij}(\mathbf{x}, \bar{\mathbf{x}}, \bar{t})}{\partial \bar{t}} f_j(\bar{\mathbf{x}}, t - \bar{t}) d\bar{t} + U_{ij}(\mathbf{x}, \bar{\mathbf{x}}, 0) f_j(\bar{\mathbf{x}}, t) \right] d\mathbf{l}(\bar{\mathbf{x}}) - \int_D \left[ \int_0^t \frac{\partial P_{ij}(\mathbf{x}, \bar{\mathbf{x}}, \bar{t})}{\partial \bar{t}} u_j(\bar{\mathbf{x}}, t - \bar{t}) d\bar{t} + P_{ij}(\mathbf{x}, \bar{\mathbf{x}}, 0) u_j(\bar{\mathbf{x}}, t) \right] d\mathbf{l}(\bar{\mathbf{x}}), \quad (23)$$

where  $\hat{u}_{ij}(\mathbf{x}, \bar{\mathbf{x}}, \bar{t}) \equiv \mathcal{L}^{-1}[\hat{U}_{ij}(\mathbf{x}, \bar{\mathbf{x}}, s)]$  and  $P_{ij}(\mathbf{x}, \bar{\mathbf{x}}, \bar{t}) \equiv \mathcal{L}^{-1}[\hat{P}_{ij}(\mathbf{x}, \bar{\mathbf{x}}, s)]$ . Here we have used the convolution and the derivative properties of the Laplace transform.<sup>45,46</sup>

## Appendix A2. The fundamental solutions in the time domain for the standard solid model

Here we show how to obtain the expressions of the fundamental solutions in the time domain, namely  $U_{ij}(\mathbf{x}, \bar{\mathbf{x}}, \bar{t})$  and  $P_{ij}(\mathbf{x}, \bar{\mathbf{x}}, \bar{t})$ . As shown in Appendix A1, the stress  $\sigma_{ij}$  and the strain  $\varepsilon_{ij}$  tensors are decomposed into the hydrostatic and deviatoric parts. For viscoelastic materials made of polymers such as elastomers and

gels, the response to the hydrostatic pressure acts like purely elastic materials. We thus write

$$\sigma_{kk} = 3K\varepsilon_{kk} \quad (24)$$

for the hydrostatic part.

We consider the standard solid (Zener) model which consists of a spring connected in parallel with a Maxwell element (a spring connected in series with a viscous damper). That means we can construct the following relations between the different components of stresses and strains. The superscript 'Ma' is used to represent the Maxwell element; 'e2' and 'η' are respectively for the elastic and the viscous component of the Maxwell element, and 'e1' for the elastic part that is connected in series with the Maxwell element. Hence for the deviatoric part we have

$$s_{ij} = s_{ij}^{\text{Ma}} + s_{ij}^{\text{e1}} \quad (25)$$

and

$$e_{ij} = e_{ij}^{\text{Ma}} = e_{ij}^{\text{e1}}. \quad (26)$$

The Maxwell element gives the following relations as

$$s_{ij}^{\text{Ma}} = s_{ij}^{\text{e2}} = s_{ij}^{\eta} \quad (27)$$

$$e_{ij}^{\text{Ma}} = e_{ij}^{\text{e2}} + e_{ij}^{\eta}. \quad (28)$$

The constitutive relations for each component are given as

$$s_{ij}^{\text{e1}} = 2Ge_{ij}^{\text{e1}}, \quad s_{ij}^{\text{e2}} = 2G_1 e_{ij}^{\text{e2}}, \quad s_{ij}^{\eta} = 2\eta \dot{e}_{ij}^{\eta}. \quad (29)$$

Using the above relations we end up with the constitutive relation for the whole deviatoric part of the Zener model given as

$$s_{ij} + \frac{\eta}{G_1} \dot{s}_{ij} - 2Ge_{ij} - \frac{2\eta(G + G_1)}{G_1} \dot{e}_{ij} = 0. \quad (30)$$

In terms of the generalized differential form of the constitutive relation in eqn (15), we get for the Zener model

$$p_0 = 1, p_1 = \frac{\eta}{G_1}, q_0 = 2G, q_1 = \frac{2\eta(G + G_1)}{G_1}, \quad (31)$$

and the other coefficients of  $p_l$  and  $q_m$  being vanishing. Next, we impose the Laplace transform to the differential form of the constitutive relation (30), we end up with the constitutive relation in Laplace space given as

$$S_{ij}(s) = \frac{q_0 + sq_1}{1 + sp_1} E_{ij}(s) \quad (32)$$

where

$$S_{ij}(s) \equiv \int_0^\infty s_{ij}(t) \exp(-st) dt \quad (33)$$

and

$$E_{ij}(s) \equiv \int_0^\infty e_{ij}(t) \exp(-st) dt. \quad (34)$$

Including the hydrostatic part, we have the full constitutive relation in the Laplace space

$$\Sigma_{ij}(s) = 3KE_{kk}\delta_{ij} + \frac{q_0 + sq_1}{1 + sp_1} E_{ij}(s) \quad (35)$$



where

$$\Sigma_{ij}(s) \equiv \int_0^{\infty} \sigma_{ij}(t) \exp(-st) dt. \quad (36)$$

Hence we can define the bulk modulus and the shear modulus in Laplace space as

$$\hat{K}(s) = K, \hat{G}(s) = \frac{q_0 + sq_1}{2(1 + sp_1)} \quad (37)$$

To obtain the fundamental solutions  $U_{ij}(\mathbf{x}, \bar{\mathbf{x}}, t) \equiv \mathcal{L}^{-1}[\hat{U}_{ij}(\mathbf{x}, \bar{\mathbf{x}}, s)]$  and  $P_{ij}(\mathbf{x}, \bar{\mathbf{x}}, t) \equiv \mathcal{L}^{-1}[\hat{P}_{ij}(\mathbf{x}, \bar{\mathbf{x}}, s)]$ , what we need to do is to perform the inverse Laplace transform of  $\hat{J}_1(s), \hat{J}_2(s), \hat{J}_3(s)$  and  $\hat{J}_4(s)$  using the expressions of  $\hat{K}(s)$  and  $\hat{G}(s)$  in (37), we then obtain

$$\begin{aligned} J_1(t) &\equiv \mathcal{L}^{-1}[\hat{J}_1(s)] \\ &= 2 \left[ \frac{6K + 7q_0}{q_0(3K + 2q_0)} + \frac{2(p_1q_0 - q_1)}{q_0q_1} \exp\left(-\frac{q_0}{q_1}t\right) \right. \\ &\quad \left. + \frac{6(p_1q_0 - q_1)}{(3K + 2q_0)(3Kp_1 + 2q_1)} \exp\left(-\frac{3K + 2q_0}{3Kp_1 + 2q_1}t\right) \right] \end{aligned} \quad (38)$$

$$\begin{aligned} J_2(t) &\equiv \mathcal{L}^{-1}[\hat{J}_2(s)] \\ &= 2 \left[ \frac{6K + q_0}{q_0(3K + 2q_0)} + \frac{2(p_1q_0 - q_1)}{q_0q_1} \exp\left(-\frac{q_0}{q_1}t\right) \right. \\ &\quad \left. - \frac{6(p_1q_0 - q_1)}{(3K + 2q_0)(3Kp_1 + 2q_1)} \exp\left(-\frac{3K + 2q_0}{3Kp_1 + 2q_1}t\right) \right] \end{aligned} \quad (39)$$

$$\begin{aligned} J_3(t) &\equiv \mathcal{L}^{-1}[\hat{J}_3(s)] \\ &= \frac{9K(-p_1q_0 + q_1) \exp\left(-\frac{3K + 2q_0}{3Kp_1 + 2q_1}t\right) + (6K + 7q_0)(3Kp_1 + 2q_1)}{(3K + 2q_0)(3Kp_1 + 2q_1)} \end{aligned} \quad (40)$$

$$\begin{aligned} J_4(t) &\equiv \mathcal{L}^{-1}[\hat{J}_4(s)] \\ &= \frac{(6K + q_0)(3Kp_1 + 2q_1) + 9K(p_1q_0 - q_1) \exp\left(-\frac{3K + 2q_0}{3Kp_1 + 2q_1}t\right)}{(3K + 2q_0)(3Kp_1 + 2q_1)} \end{aligned} \quad (41)$$

At  $t = 0$ , the functions are given as

$$J_1(0) = \frac{2(3K + 7G_{12})}{G(3K + 4G_{12})} \quad (42)$$

$$J_2(0) = \frac{2(3K + G_{12})}{G(3K + 4G_{12})} \quad (43)$$

$$J_3(0) = \frac{2(3K + 7G_{12})}{3K + 4G_{12}} \quad (44)$$

$$J_4(0) = \frac{2(3K + G_{12})}{3K + 4G_{12}} \quad (45)$$

where  $G_{12} \equiv G + G_1$ .

When  $t \rightarrow \infty$ , we have

$$J_1(\infty) = \frac{2(3K + 7G)}{G(3K + 4G)}, \quad (46)$$

$$J_2(\infty) = \frac{2(3K + G)}{G(3K + 4G)}, \quad (47)$$

$$J_3(\infty) = \frac{2(3K + 7G)}{3K + 4G}, \quad (48)$$

$$J_4(\infty) = \frac{2(3K + G)}{3K + 4G}. \quad (49)$$

## Acknowledgements

TSC gratefully acknowledges financial support from the Research Council of Norway (Project No. 315110). TSC thanks Christian Pedersen for the fruitful discussions and the referees of the paper for the inspiring comments to help to improve the manuscript.

## References

- 1 S. J. Park, B. M. Weon, J. S. Lee, J. Lee, J. Kim and J. H. Je, *Nat. Commun.*, 2014, **5**, 1–7.
- 2 B. Andreotti and J. H. Snoeijer, *Annu. Rev. Fluid Mech.*, 2020, **52**, 285–308.
- 3 R. W. Style and E. R. Dufresne, *Soft Matter*, 2012, **8**, 7177–7184.
- 4 A. Carré, J.-C. Gastel and M. E. R. Shanahan, *Nature*, 1996, **379**, 432–434.
- 5 T. Kajiya, A. Daerr, T. Narita, L. Royon, F. Lequeux and L. Limat, *Soft Matter*, 2013, **9**, 454–461.
- 6 S. Karpitschka, S. Das, M. Van Gorcum, H. Perrin, B. Andreotti and J. H. Snoeijer, *Nat. Commun.*, 2015, **6**, 1–7.
- 7 M. Van Gorcum, B. Andreotti, J. H. Snoeijer and S. Karpitschka, *Phys. Rev. Lett.*, 2018, **121**, 208003.
- 8 S. I. Tamim and J. B. Bostwick, *Phys. Rev. E*, 2021, **104**, 1–10.
- 9 R. W. Style, R. Boltysanskiy, Y. Che, J. S. Wettlaufer, L. A. Wilen and E. R. Dufresne, *Phys. Rev. Lett.*, 2013, **110**, 1–5.
- 10 C. Creton and M. Ciccotti, *Rep. Prog. Phys.*, 2016, **79**, 046601.
- 11 B. Corominas-Murtra and N. I. Petridou, *Front. Phys.*, 2021, **9**, 1–17.
- 12 X. Shi, Z. Liu, L. Feng, T. Zhao, C.-Y. Hui and S. Zhang, *Phys. Rev. X*, 2022, **12**, 021053.
- 13 R. Pericet-Cámara, A. Best, H. J. Butt and E. Bonaccorso, *Langmuir*, 2008, **24**, 10565–10568.
- 14 Y. S. Yu, *Appl. Math. Mech. (Engl. Ed.)*, 2012, **33**, 1095–1114.
- 15 R. W. Style, A. Jagota, C. Y. Hui and E. R. Dufresne, *Annu. Rev. Condens. Matter Phys.*, 2017, **8**, 99–118.



- 16 J. C. Fernandez-Toledano, T. D. Blake, P. Lambert and J. De Coninck, *Adv. Colloid Interface Sci.*, 2017, **245**, 102–107.
- 17 G. R. Lester, *J. Colloid Sci.*, 1961, **16**, 315–326.
- 18 A. I. Rusanov, *Colloid J. USSR*, 1975, **37**(4), 614–622.
- 19 Y. S. Yu and Y. P. Zhao, *J. Colloid Interface Sci.*, 2009, **339**, 489–494.
- 20 R. Pericet-Camara, G. K. Auernhammer, K. Koynov, S. Lorenzoni, R. Raiteri and E. Bonaccorso, *Soft Matter*, 2009, **5**, 3611–3617.
- 21 E. R. Jerison, Y. Xu, L. A. Wilen and E. R. Dufresne, *Phys. Rev. Lett.*, 2011, **106**, 1–4.
- 22 L. Limat, *Eur. Phys. J. E: Soft Matter Biol. Phys.*, 2012, **35**, 1–13.
- 23 J. Bico, É. Reyssat and B. Roman, *Annu. Rev. Fluid Mech.*, 2018, **50**, 629–659.
- 24 R. W. Style and Q. Xu, *Soft Matter*, 2018, **14**, 4569–4576.
- 25 A. Marchand, S. Das, J. H. Snoeijer and B. Andreotti, *Phys. Rev. Lett.*, 2012, **109**, 1–5.
- 26 A. Pandey, B. Andreotti, S. Karpitschka, G. J. Van Zwieten, E. H. Van Brummelen and J. H. Snoeijer, *Phys. Rev. X*, 2020, **10**, 31067.
- 27 C. Y. Hui and A. Jagota, *Proc. R. Soc. A*, 2014, **470**, 20140085.
- 28 L. A. Lubbers, J. H. Weijs, L. Botto, S. Das, B. Andreotti and J. H. Snoeijer, *J. Fluid Mech.*, 2014, **747**, R1.
- 29 J. Dervaux and L. Limat, *Proc. R. Soc. A*, 2015, **471**, 20140813.
- 30 Z. Cao and A. V. Dobrynin, *Macromolecules*, 2015, **48**, 443–451.
- 31 C. Y. Hui and A. Jagota, *J. Polym. Sci., Part B: Polym. Phys.*, 2016, **54**, 274–280.
- 32 D. Guan, E. Charlaix and P. Tong, *Phys. Rev. Lett.*, 2020, **124**, 188003.
- 33 G. Pu and S. J. Severtson, *Langmuir*, 2012, **28**, 10007–10014.
- 34 M. C. Lopes and E. Bonaccorso, *Soft Matter*, 2012, **8**, 7875–7881.
- 35 F. Mugele and J.-C. Baret, *J. Phys.: Condens. Matter*, 2005, **17**, R705.
- 36 C. Pozrikidis, *Boundary Integral and singularity methods for linearized flow*, Cambridge University Press, Cambridge, 1992.
- 37 J. D. McGraw, T. S. Chan, S. Maurer, T. Salez, M. Benzaquen, E. Raphaël, M. Brinkmann and K. Jacobs, *Proc. Natl. Acad. Sci. U. S. A.*, 2016, **113**, 1168.
- 38 T. S. Chan, J. D. McGraw, T. Salez, R. Seemann and M. Brinkmann, *J. Fluid Mech.*, 2017, **828**, 271–288.
- 39 X. Y. Zhu, W. Q. Chen, Z. Y. Huang and Y. J. Liu, *Eng. Anal. Bound Elem.*, 2011, **35**, 170–178.
- 40 C. G. Panagiotopoulos, V. Mantič and T. Roubíček, *Int. J. Solids Struct.*, 2014, **51**, 2261–2271.
- 41 R. Shuttleworth, *Proc. Phys. Soc. Sect. A*, 1950, **63**, 444.
- 42 B. Andreotti and J. H. Snoeijer, *EPL*, 2016, **113**, 66001.
- 43 R. Masurel, M. Roché, L. Limat, I. Ionescu and J. Dervaux, *Phys. Rev. Lett.*, 2019, **122**, 1–6.
- 44 M. Schanz and L. Gaul, *Appl. Mech. Rev.*, 1993, **46**, S41–S46.
- 45 S. S. Lee, Y. S. Sohn and S. H. Park, *Eng. Anal. Bound Elem.*, 1994, **13**, 211–217.
- 46 S. Syngellakis, *Eng. Anal. Bound Elem.*, 2003, **27**, 125–135.
- 47 J. Dervaux, M. Roché and L. Limat, *Soft Matter*, 2020, **16**, 5157–5176.

